Silicon Heterojunction Solar Cells Featuring Localized Front Contacts

Smits, Sebastian; Zhao, Yifeng; Procel Moya, Paul; Mazzarella, Luana; Isabella, Olindo

DOI
10.1002/solr.202400898

Publication date
2025

Document Version
Final published version

Published in
Solar RRL

Citation (APA)
Smits, S., Zhao, Y., Procel Moya, P., Mazzarella, L., & Isabella, O. (2025). Silicon Heterojunction Solar Cells Featuring Localized Front Contacts. *Solar RRL*, *9*(7), Article 2400898. https://doi.org/10.1002/solr.202400898

Solar RRL
www.solar-rrl.com

Silicon Heterojunction Solar Cells Featuring Localized Front Contacts

Sebastian Smits, Yifeng Zhao, Paul Procel Moya, Luana Mazzarella, and Olindo Isabella*

Throughout the development of silicon heterojunction (SHJ) solar cells, the transparent conductive oxide has been regarded as an essential component of their front electrode, facilitating lateral charge transport of photogenerated carriers toward the front metal grid fingers. In rear junction (RJ)-SHJ solar cells, the (*n*)c-Si bulk is known to support the lateral electron transport at maximum power point injection level, provided that the contact resistance of the front contact stack is sufficiently low. This enables experimental RJ-SHJ solar cell architectures featuring a localized front carrier-selective passivating contact exclusively covering the area contacted by the metal grid. Herein, a top-down approach to the synthesis of this type of architecture is studied and its optical and electrical performance applied to different (*n*)-type contacts are investigated. Additionally, the potential of the localized contact architecture through Cu-plated RJ-SHJ solar cells is demonstrated. These solar cell demonstrators feature high short-circuit current density of 40.5 mA cm^{-2}, without significantly compromising their open-circuit voltage or fill factor, enabling efficiencies well above 23%, a 2%$_{abs}$ improvement compared to their state before localization of the front contact.

1. Introduction

Decades of development are behind the combination of intrinsic and doped hydrogenated amorphous or nanocrystalline silicon layers (a-Si:H or nc-Si:H and/or its alloys, respectively) to form a contact that concurrently chemically passivates the c-Si surface and selectively allows the collection of negative or positive charge carriers. This has resulted in front/back-contacted (FBC)-silicon heterojunction (SHJ) solar cells demonstrating high power conversion efficiency (η) of 26.81%.[1] Much effort in the improvement of SHJ solar cell technology is focused on the optical performance by optimizing both the front and rear carrier-selective passivating contact (CSPC) layer thicknesses, allowing SHJ solar cell efficiencies to reach 24.18% in our lab.[2,3] Due to the defective nature of the intrinsic and doped a-Si:H layers that form the CSPCs of the solar cell, a significant portion of light is absorbed without contributing to usable current in the FBC configuration.[4] Additionally, the transparent conductive oxide (TCO) layers used to contact the solar cells need to fulfill two roles simultaneously, being an electrically conductive material for lateral transport while acting as an optically transparent antireflective coating (ARC). In general, these properties compete with one another, as an increase of doping concentration in the TCO material may benefit its conductivity but simultaneously reduces transparency in the infrared due to free carrier absorption.[5] As a consequence, η of SHJ solar cells compared to other c-Si based technologies remains limited by its (J_{sc}).[6,7] This has sparked the development of ultrathin front-side CSPCs aimed to reduce fraction of the light lost to parasitic light absorption without compromising the charge carrier transport.[3,8,9] Alternatively, back-contacted architectures based on heterojunction technology offer a promising pathway forward to reduce parasitic light absorption and remove shading losses of the front metal grid.[10] Nevertheless, the single-side contacted designs come with industrial challenges such as increased processing complexity, higher probability of shunt paths, and wafer bowing from one-sided metallization.[11,12]

Bivour et al. offered a new perspective on the requirements of the front TCO, after demonstrating that for (*n*)-type c-Si substrates, lateral transport of the negative charge carriers partially takes place within the c-Si bulk under operating conditions.[13] This enabled the usage of less conductive and more transparent front TCOs boosting J_{sc} despite limited loss of fill factor (FF).[14] Haschke et al. elaborated on that work by highlighting that not alone the conductivity of the charge carriers in the c-Si bulk, but also the less-resistive coupling between the bulk and the front TCO can promote lateral charge transport within the bulk.[15] Combined, both aforementioned developments provide the rationale to separate the functionality of the front contact into

---

S. Smits, Y. Zhao, P. Procel Moya, L. Mazzarella, O. Isabella
Photovoltaic Materials and Devices Group
Delft University of Technology
Mekelweg 4, 2628 CD Delft, The Netherlands
E-mail: s.smits-1@tudelft.nl

The ORCID identification number(s) for the author(s) of this article can be found under https://doi.org/10.1002/solr.202400898.

DOI: 10.1002/solr.202400898

two regions, namely the contact regions underneath the front metal grid and the window openings. Through localization of negative charge carrier extraction exclusively underneath the area shaded by the front metal grid, the layers in the window openings may be selected regardless of their electrical conductivity, should the c-Si surface passivation remain guaranteed. Pioneering attempts of this concept include SHJ solar cells that either omitted the front TCO,[16] featured a localized front TCO under the metal grid,[17] or employed partially localized front TCO and doped layers covering 50% of the front area.[18] In these works, the localized contact concept was found mostly viable for the rear junction (RJ) configurations. However, reported efficiencies remained below state of the art as a consequence of a compromised FF.

The aforementioned works have relied on bottom-up approaches to pattern the contact layers, which involved the deposition of the contact layers through a shadow mask followed by Ag screen-printed metallization. An inherent limitation of this approach, however, is the resolution of the front contacts which is limited by the openings of the shadow mask and the minimal attainable screen-printed finger width and pitch ($\geq$30 µm and 1.85 mm, respectively).[18] In this work, an alternative top-down method to fabricate the localized front contact architecture is developed, leveraging the front metal grid as a mask for local etching. Utilizing the ultranarrow (15 µm) features of our previously developed Cu-plating metallization scheme,[19,20] the top-down method can realize localized front contacts at a significantly reduced pitch of 930 µm. The developed process flow was systematically evaluated through solar cell demonstrators featuring localized front contacts based on a range of different (*n*)-type CSPC layer stacks, keeping previously optimized rear (*p*)-type CSPC constant.[21] The optical performance of the most promising localized structure is compared to a similar structure equipped with a traditional full area contacted SHJ architecture, to assess the respective parasitic light absorption losses. Finally, by comparison of the external parameters, the potential of the solar cells featuring localized front contacts is demonstrated, and the implications of these findings are discussed.

2. Results and Discussion

2.1. Top-down Process Flow

The top-down process flow, depicted in **Figure 1**, primarily consists of the regular fabrication of SHJ solar cell precursors. Following their metallization, the front TCO and (*n*)-doped layers are selectively etched from the window openings. Because of the risk of Cu-contamination of plasma tools, the self-masked TCO and (*n*)-doped layer patterning steps are restricted to wet chemical methods. Solutions based on strong halogen acids, such as HCl, are known to etch tin-doped indium oxide (ITO), the material used as the front TCO in this study, effectively.[22] Experiments with diluted (1:5 $HCl{:}H_2O$) solutions resulted in a controllable etching rate, removing 30 nm ITO from a textured (*n*)c-Si substrate within 90 s. When masked by the front metal grid, however, detrimental etching undercut caused the fingers to delaminate from the sample before the front ITO was completely removed (Figure S1, Supporting Information). Therefore, the process was established using undiluted fuming (37%) HCl as the etchant, which required only 12 s to remove the 30-nm-thick ITO at room temperature, without resulting in finger delamination (Figure 1b). Additionally, the mechanical stability of the fingers was assessed by performing the tape test described in ASTM D3359-23 on a solar cell with and without patterned TCO.[23] Since both samples passed the test, we conclude the mechanical stability to be not significantly compromised by the TCO patterning step.

Figure 2a depicts a cross-sectional scanning electron microscopy (SEM) image of one of the front grid finger contacts of a solar cell sample in the final state of Figure 1. The cut from the chip-dicing machine remained too rough to identify the 100-nm-thick Ag seed layer and 30-nm-thick localized TCO traces under the Cu finger. Therefore, additional stripping of all Ag and Cu using HNO_3 was performed, after which a top-down SEM image was captured depicted in Figure 2b. The darker regions in Figure 2b correspond to the window openings where the nonconductive double-layer ARC (DLARC) was deposited. As this layer had been deposited after metallization, the border

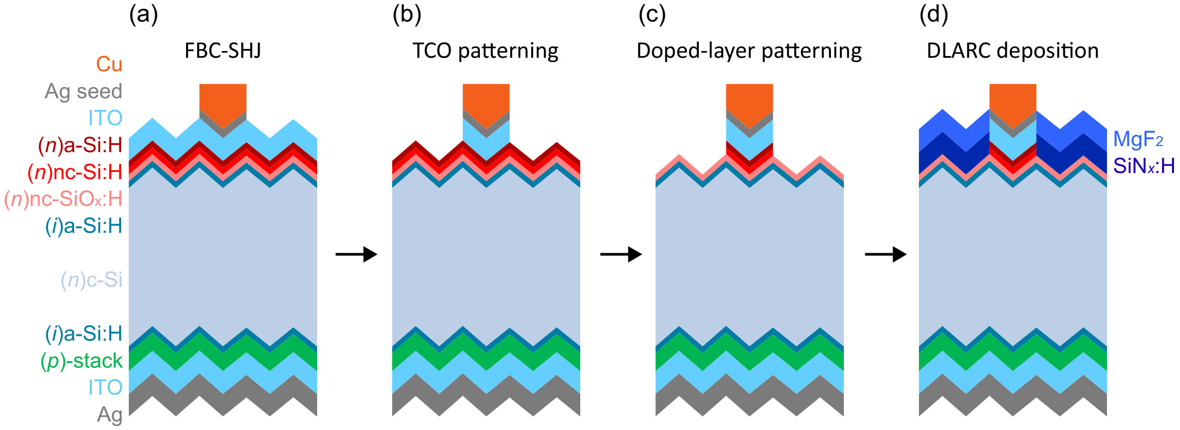

Figure 1. a–c) Schematic representation of the self-aligned wet chemical process flow to synthesize the FBC-SHJ solar cells featuring localized front contacts. Layer thicknesses are not to scale. In step d), we omit the hydrogenated silicon nitride ($SiN_x{:}H$) film coating the Cu-plated finger due to its negligible thickness as compared to the finger height.

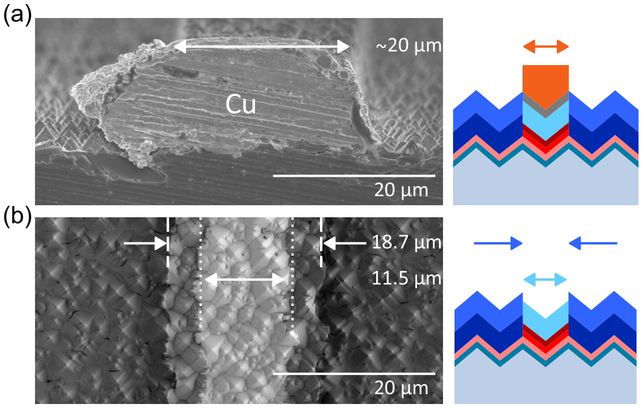

Figure 2. a) SEM images of the cross section of a Cu finger of a localized solar cell corresponding to Figure 1d. b) A top-down view after wet chemical removal of the metal finger.

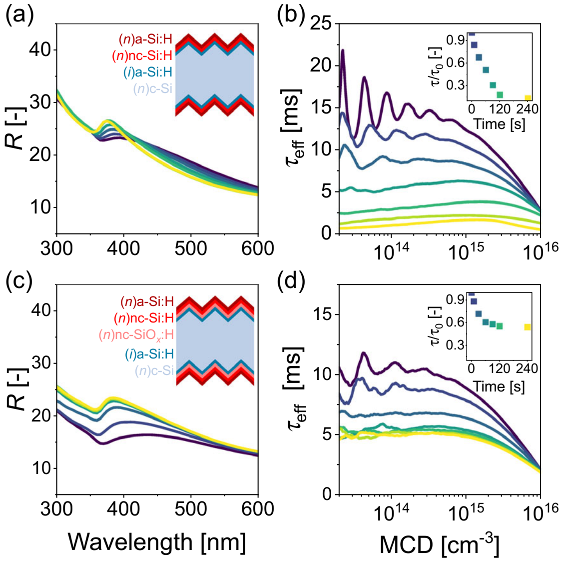

Figure 3. Reflectance and photoconductance measurements of symmetric test structures a,b) without and c,d) with 8 nm (*n*)nc-SiO$_x$:H stopping layer, respectively. Dark-to-light traces represent the cumulative exposure time to KOH ranging from 0 to 240 s. Insets represent the lifetime evaluated at 10^{15} cm^{-3} as a function of etching time, normalized by its value before etching.

of the darker region outlines the width of the Cu finger before it was stripped. The bright region in Figure 2b corresponds to the patterned ITO located under the front metal grid. The difference in width of the traces of ITO and Cu reveals still the presence of undercut, resulting from the self-masked wet chemical patterning step, despite the mechanical stability of the fingers. Reportedly, the addition of oxidizing agents such as $FeCl_3$ acts as a catalyst and reduces the degree of undercut.[24] However, in our context the addition of oxidizing agents makes the solution corrosive to Cu and Ag. Possibly, TCO etching step may be more controllable with the use of organic acids such as oxalic acid, which may simultaneously clean the sample from residual metal ions through chelation.[25,26] Oxalic acid has, however, been reported to affect the stoichiometry of ITO due to the different etch rates of SnO_2 and In_2O_3, affecting the electrical properties of ITO and etching uniformity.[25,27]

The next step involves the wet chemical etching of the (*n*)-doped layer stack from the window openings (Figure 1c). As previously pointed out by Greil et al. etching uniformity is challenging when wet chemical etching thin-film silicon layers.[28] However, given that there is no selectivity of the etching solution between doped and intrinsic silicon thin-films, the wet etching method may negatively affect the interfacial passivation quality that can be detrimental to the electrical performance of the localized solar cell. To circumvent this issue, we introduced a thin transparent ($E_{04} = 2.26$ eV) (*n*)-type hydrogenated nanocrystalline silicon oxide (nc-SiO$_x$:H) layer in between the intrinsic layer and our regular (*n*)-type (nc-Si:H + a-Si:H) contact stack.[8] This layer, which we will refer to as the stopping layer, allows overetching of the (*n*)-type stack to ensure its complete removal from the window openings without affecting the intrinsic layer underneath. Diluted alkaline solutions such as tetra-methylammonium hydroxide (TMAH)(5%) or potassium hydroxide (KOH) (1%) are commonly used to etch silicon thin-films. A primary dip in diluted HF was used to remove any oxide from the previous a-Si:H/ITO interface, to ensure a more uniform etch. Reportedly, TMAH solutions result in smoother interfaces after etching, suggesting more uniform etching compared to KOH.[29] Besides, being based on an organic compound, TMAH is also favorable over KOH from an ion contamination point of view, known to cause long-term potential-induced degradation.[30] Despite these advantages, room-temperature experiments resulted in more controllable etching with KOH solutions (Figure S2, Supporting Information).

The effectiveness of the (*n*)nc-SiO$_x$:H stopping layer was monitored by exposing symmetric test structures with and without (*n*)nc-SiO$_x$:H (depicted in **Figure 3**) to KOH for various durations. Comparing the spectrophotometry reflectance measurements in Figure 3a,c, a gradual change of the short-wavelength reflectance can be observed throughout the exposure time for the sample without stopping layer, whereas for the sample with stopping layer this change seems to be limited up to 60 s of KOH exposure. Similarly, the effective minority carrier lifetime measurements in Figure 3b,d demonstrate the same gradual degradation of minority carrier lifetime for the sample without the stopping layer, whereas for the sample with the stopping layer the relative degradation is limited to roughly 40% after 60 s KOH exposure. Moreover, the increased degradation of effective minority carrier lifetime in both the low- and high-injection regime of Figure 3b indicates the formation of defects after extended exposure to the KOH solution.[31] In Figure 3d, however, the lifetime reduction mainly takes place in the low-injection regime with limited change at high-injection level, suggesting that Shockley–Read–Hall recombination from defect formation at the front c-Si interface is not the main mechanism. Rather, the limited lifetime decrease in this case may be attributed to the reduced front surface field after removal of the (*n*)nc-Si:H + (*n*)a-Si:H contact stack from the window openings.[31,32] Therefore, 8 nm (*n*)nc-SiO$_x$:H between the (*i*)a-Si:H layer and the to-be-patterned contact layer stack is sufficient to act as a barrier inhibiting the etching of the (*i*)a-Si:H layer. Additional experiments showed similar results for samples based on 4-nm-thick (*n*)nc-SiO$_x$:H (Figure S3, Supporting Information).

Besides providing lateral transport of charge carriers, the front TCO also acts as an ARC mitigating the large difference of refractive index between silicon and air.[33] Therefore, following the removal of the contact layers, a more transparent replacement DLARC is deposited to promote light in-coupling (Figure 1d). With the patterning of the (*n*)-doped contact layer stack, the window opening regions of the front interface contain fewer active dopants than previously present in the (*n*)-type CSPC, as in these regions only 8-nm-thick (*n*)nc-SiO$_x$:H remains. Because of the reduction of the front surface field in these regions, hole concentrations become less suppressed near the front c-Si interface, degrading the passivation quality of the solar cell.[32] In order to enhance the front surface field, a 70-nm-thick SiN$_x$:H ARC is deposited via plasma-enhanced chemical vapor deposition (PECVD) in a dedicated PECVD reactor. The fixed positive charges in the SiN$_x$:H film are known to attract electrons near the c-Si surface, inducing a field effect that restores passivation of the front c-Si interface.[34] In conjunction with SiN$_x$:H, an additional 100-nm-thick MgF$_2$ optical capping layer is deposited through electron beam physical vapor deposition to complete the DLARC.[35] The optimal thicknesses of the respective ARC layers were determined by optical simulations (Figure S4, Supporting Information).

2.2. Internal Series Resistance

Charge carrier transport within a solar cell featuring the localized front contact architecture is expected to differ from the transport in the traditional architecture, as negative charge carrier collection can no longer occur through the front TCO in the window opening regions of the cell. Following the methodology described in ref. [36], using *J*–*V* and Suns–V_{oc} characteristics, R_S was determined before and after patterning of the front TCO. **Figure 4** depicts the evaluation of R_S for solar cells featuring various (*n*)-type contact stacks as schematically depicted in the corresponding diagrams above the plot.

The first batch depicted in Figure 4 is based on a 4-nm-thick (*n*)nc-SiO$_x$:H stopping layer combined with a variable thickness of (*n*)a-Si:H. Despite good initial performance, the R_S significantly increases after patterning of the front TCO, depending on the (*n*)a-Si:H thickness. This demonstrates that for these structures, lateral carrier transport relies heavily on a conductive front TCO in the traditional architecture. Substitution of the (*n*)a-Si:H with a variable thickness of (*n*)nc-Si:H is capable of realizing similar performance before TCO patterning, but results in notable reduction of R_S increase after TCO patterning. These (*n*)-type layer stacks, however, require impractically thick layers of over 20 nm to minimize the change of R_S, challenging the uniformity of the subsequent doped-layer patterning step. Upon the combination of our regular 3 nm nc-Si:H + 2 nm a-Si:H (*n*)-type stack with a variable thickness of (*n*)nc-SiO$_x$:H stopping layer, both before but more notably after patterning, R_S is first negatively affected by the incorporation of (*n*)nc-SiO$_x$:H regardless of its thickness. Interestingly, however, a significant reduction of R_S increase after TCO patterning is observed for a (*n*)nc-SiO$_x$:H thickness of 8 nm, outperforming the same (*n*)-type stack without the stopping layer. Moreover, despite identical properties of the c-Si wafer and metallization pitch and width throughout all samples presented in Figure 4, several localized designs feature R_S below 1 Ω cm^2. Therefore, we demonstrate that the lateral conductivity of the c-Si bulk under operating conditions is able to replace that of the front TCO, facilitating carrier collection without introducing significant resistive losses in several cases.

Comparing the results presented in Figure 4, we observe that the properties of the (*n*)-type contact layers have a large influence on the R_S of solar cell after its front TCO is localized. The decreasing trends upon thicker a-Si:H or nc-Si:H layers suggest

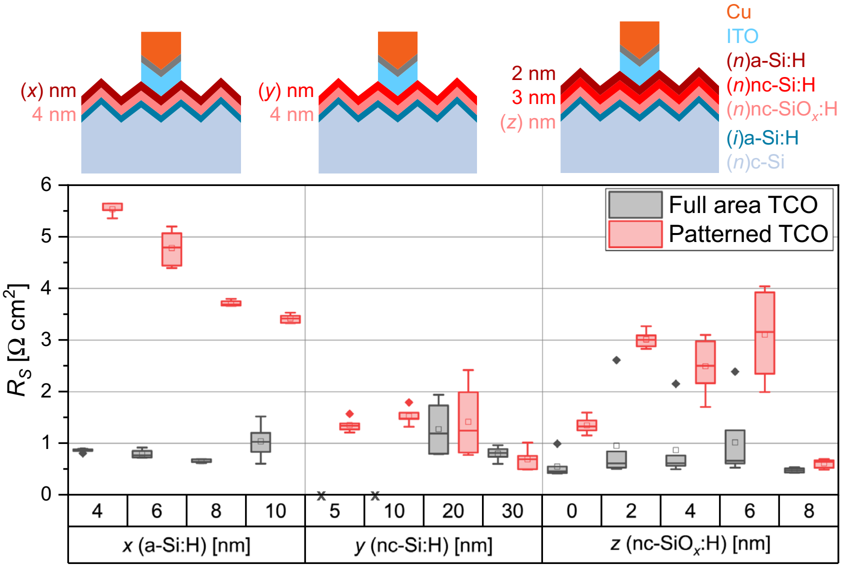

Figure 4. Internal series resistance (R_S) obtained from 1-Sun illuminated current–voltage (*J*–*V*) and flash-illuminated open-circuit voltage (Suns–V_{oc}) measurements before and after patterning of the front TCO for various (*n*)-type contact stacks. Schematic representations of the corresponding solar cells after TCO patterning are depicted above the plotted data. Crosses indicate missing data.

that contact resistivity (ρ_c), which generally reduces with thicker layers by reduction of the activation energy (E_a),[8] plays an important role. As proposed by Haschke et al. sufficient electrical coupling between the front TCO and c-Si bulk enables significant lateral transport within the c-Si bulk.[15] Thus, reduction of ρ_c below a certain threshold removes the need of a conductive front TCO layer in the first place, minimizing the increase of R_S after the localization of the front contact. This insight on the role of ρ_c is consistent with previous findings from Sai et al. where the ρ_c was identified as a critical parameter for the FF of their TCO-less solar cells.[17] Likewise, the results in Figure 4 demonstrate that when all negative charge carrier collection from the c-Si bulk takes place exclusively through the area underneath the front metal grid, the contribution of ρ_c to R_S is amplified.

Finally, the difference between the bilayer (n)-type stack with or without a (n)nc-SiO$_x$:H *stopping* layer corroborates the aforementioned notion. After all, incorporating (n)nc-SiO$_x$:H, featuring two magnitudes lower dark conductivity compared to (n)nc-Si:H, is expected to increase ρ_c of the stack.[8,37] In fact, the sudden reduction of R_S before and more notably after TCO patterning when an 8-nm-thick (n)nc-SiO$_x$:H stopping layer is used suggests a competing effect responsible for lowering the ρ_c of the stack in this instance. This is in line with the delayed nucleation of nanocrystals observed previously during the development of the (n)nc-SiO$_x$:H layer re-used in the current work ((n) nc-SiO$_x$:H-2 in ref. [8]). At that time, comparable FF of around 79% was demonstrated between solar cells featuring either 8 nm (n)nc-SiO$_x$:H or 3 nm (n)nc-Si:H, whereas solar cells featuring 3 nm (n)nc-SiO$_x$:H yielded 76% FF. Additionally, the oxygen alloyed in the stopping layer may in turn promote nanocrystalline growth in the subsequently deposited (n)nc-Si:H layer, similar to how interfaces treated with CO$_2$-diluted plasmas are reported to prompt nucleation in (p)-type stacks.[38,39] A more in-depth study of the structural and electrical properties of (n)-type stacks on top of (n)nc-SiO$_x$:H layers is needed to further clarify the trend observed in the (n)nc-SiO$_x$:H series of Figure 4. More importantly, the fact that the structures featuring 8-nm-thick stopping layer outperform identical samples without stopping layer after localization of the front contact highlights its dual functionality. Besides facilitating the wet chemical patterning of the doped layers, the stopping layer concurrently reduces the resistive losses in the localized CSPC.

2.3. Solar Cell Performance

The most promising solar cell structure from Figure 4 featuring the 8-nm + 3-nm + 2-nm-thick (n)nc-SiO$_x$:H + (n)nc-Si:H + (n) a-Si:H front contact stack was characterized spectrally to assess the optical impact of the patterning steps introduced in Figure 1b,c. **Figure 5**a depicts the measured external quantum

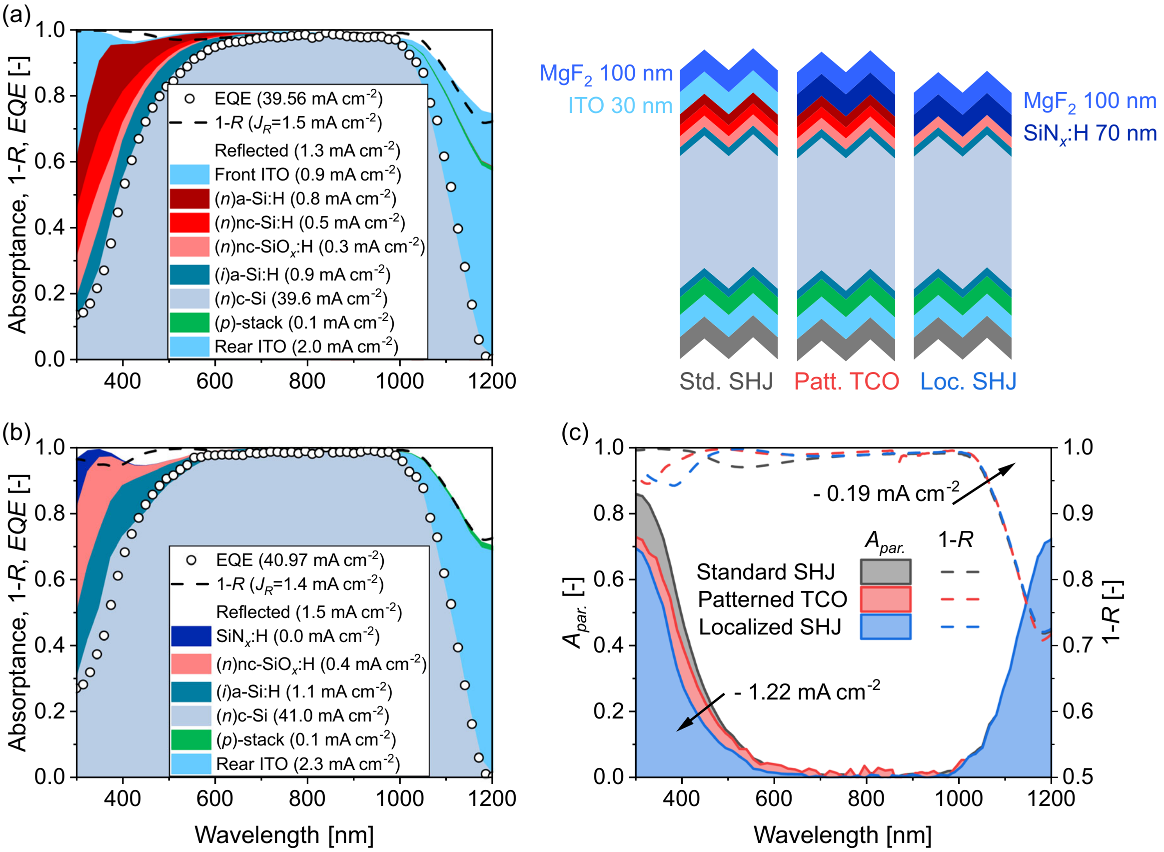

Figure 5. a) Measured EQE (open circles) and reflectance (1 − R, dashed lines) and simulated absorptance spectra corresponding to the window opening regions of the traditional and b) the localized front contact architectures, respectively. c) The derived spectral parasitic light absorption (A_{par}) and reflectance (1 − R) including that of an intermediate structure featuring a patterned TCO and full-area doped layer.

efficiency (EQE) and reflectance spectra of a reference solar cell equipped with a full-area ITO/MgF_2 DLARC. Likewise, the measurements depicted in Figure 5b correspond to a solar cell that underwent the complete process flow introduced in Figure 1. Reasonable agreement between the measured EQE and the simulated absorptance contributions[40] depicted in the background suggests the patterning steps to have cleared the window opening regions of the cells as intended. As a consequence, the EQE is improved resulting in a $J_{sc,EQE}$ gain of 1.41 mA cm^{-2}. In Figure 5c, the derived parasitic light absorptance and spectral reflectances of these solar cells are compared, together with an intermittent structure that excluded the doped-layer patterning step in Figure 1c. A small contribution of 0.19 mA cm^{-2} is distinguished, originating from the more favorable antireflective properties of the SiN_x:H-based DLARC as compared to the reference. The residual of the EQE increase is attributed to the reduction of parasitic light absorption in the window layers by 1.22 mA cm^{-2}, clearly demonstrating the optical potential of the localized front contact architecture. Moreover, the benefits of the patterning steps comfortably exceed the 0.4 mA cm^{-2} absorptance originating from the additional (*n*)nc-SiO_x:H stopping layer.

Figure 6 depicts the *J*–*V* characteristics of the champion solar cell in this study in the first (Figure 1a) and the final (Figure 1d) stage of the process flow. Comparing the characteristics in Figure 6, which correspond to the same die on the same wafer, a substantial J_{sc} boost of 3.3 mA cm^{-2} can be observed. Note that this exceeds the parasitic light absorption reduction reported in Figure 5c as reflectance is notably reduced compared to the single-layer ITO ARC of suboptimal thickness. Compared to a separate standard SHJ solar cell equipped with a ITO/MgF_2-based DLARC (dashed line in Figure 6), the 1.1 mA cm^{-2} J_{sc} advantage of the localized front contact architecture is consistent with the results from Figure 5c. Meanwhile, open-circuit voltage (V_{oc}) remains unaffected despite exposure of the Cu-metallized solar cell to various etchants and PECVD deposition of SiN_x:H at elevated temperature. The subtle improvement of V_{oc} is attributed to the enhanced front-surface field as a consequence of the fixed positive charges in SiN_x:H. Simultaneously, FF is only slightly affected as a consequence of the dual functionality of (*n*) nc-SiO_x:H, remaining nearly at 81%. Combined, the η of the solar cell is improved by almost $2\%_{abs}$, yielding a champion efficiency of 23.4% that outperforms the control SHJ by $0.7\%_{abs}$.

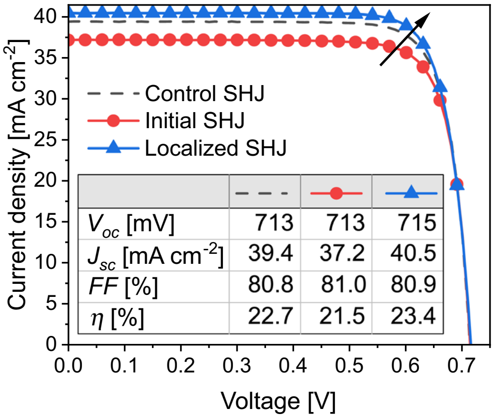

	- - -	●	▲
V_{oc} [mV]	713	713	715
J_{sc} [mA cm^{-2}]	39.4	37.2	40.5
FF [%]	80.8	81.0	80.9
η [%]	22.7	21.5	23.4

Figure 6. *J*–*V* characteristics of the champion solar cell in this study after metallization (Figure 1a) and after front contact localization and subsequent DLARC deposition (Figure 1d), (solid circles and triangles, respectively). Dashed line represents a separate control solar cell, which is structurally identical to the initial SHJ but includes a MgF_2 DLARC.

In light of these findings, new considerations can be taken into account in the design of FBC-SHJ solar cells. The results in Figure 4 demonstrate that the use of more conductive contact stacks at the expense of transparency can be justified, if in turn the lateral conductivity offered by the front TCO becomes obsolete. This drives new incentive behind the development of highly conductive CSPCs, regardless of their transparency, as besides the obvious reason of improving FF, we have shown that J_{sc} can benefit too, should it enable one to localize charge carrier extraction from the c-Si bulk. On top of that, this work also highlights the importance of low ρ_c of the front CSPC as a tool to reduce the reliance on the critical element indium.[41]

Looking ahead, the potential performance of FBC-SHJ solar cell featuring localized front contacts has recently been assessed through rigorous optoelectrical simulations, demonstrating theoretical efficiency optimum exceeding 28%.[3,42] Among other simulated architectures, the localized front contact architecture is one of the most promising FBC-SHJ solar cell designs. The current work provides a proof of concept; however, significant room for improvement remains. The electrical performance of this type of architecture is expected to benefit from reduced wafer thickness as low as 60 μm and increased wafer resistivity to 10 Ω cm. In terms of optical performance, the short-wavelength losses may further be minimized should the use of the stopping layer be circumvented and the (*i*)a-Si:H be localized too. The latter will become especially important as lately the long-term stability of the front Si—H passivating bond is challenged by the ever-increasing short-wavelength transparency of the front CSPC.[43–45] Materials to passivate the window opening regions may in turn be selected for their stability against UV-induced degradation (UVID) regardless of conductivity. Therefore, the localized front contact architecture certainly opens pathways to extend the efficiency potential of the current state-of-the-art, while possibly mitigating issues related to long-term stability and sustainability.

3. Conclusion

In this work, we have examined the possibility to rely on the lateral conductivity of the (*n*)-type c-Si to fully support negative charge carrier collection at the front contact of RJ SHJ solar cells. A top-down processing method has been developed to synthesize the localized front contact architecture by self-aligned wet chemical etching of a traditional SHJ solar cell after Cu-plating metallization. Despite the observed undercut, the TCO and (*n*)-type contact layers were patterned exclusively under the front metal grid, without finger delamination or damage to the passivating (*i*)a-Si:H layer. By comparing R_S of various structures, we found that (*n*)-type contacts stacks with likely sufficiently low ρ_c demonstrated limited increase of R_S after TCO patterning. Leveraging the dual functionality of (*n*)-type nc-SiO_x:H, we empirically demonstrated sufficient lateral conductivity within the (*n*)-type c-Si bulk to replace the full-area front TCO.

Furthermore, from EQE and spectrophotometry reflectance measurements, the fraction of the light lost to parasitic light absorption in the localized front contact architecture was found to be reduced by 1.22 mA cm^{-2} compared to reference solar cells based on the same precursors, featuring the traditional architecture. This enabled a champion localized front contact solar cell with high J_{sc} of 40.5 mA cm^{-2}, while maintaining FF near 81%. As a result, this champion solar cell yielded η of 23.4% (0.7%$_{abs}$ improvement with respect to the control), which is to the best of our current knowledge the highest obtained efficiency of a FBC-SHJ solar cell based on the localized front contact architecture. The unprecedented conservation of FF in the presented localized front contact solar cells opens new doors for low-ρ_c (n)-type CSPCs enabling high-efficiency FBC-SHJ solar cells that can reduce indium consumption and improve resilience against UVID.

4. Experimental Section

SHJ Solar Cell Fabrication: Polished 280 ± 20 μm (n)-type c-Si float-zone <100>-oriented wafers with a bulk resistivity of 3 ± 2 Ω cm were submitted to double-side random pyramidal texturing in a solution of 5% TMAH with 2.4% ALKA-TEX 8 additive from GP-Solar-GmbH. at 80 °C and stirred at 100 RPM for 15 min.[46] After texturing, all wafer substrates were submitted to three nitric acid oxidation cycles, as specified in ref. [47] The textured wafer substrates were exposed to 0.55% HF for 5 min in a Marangoni dryer setup prior to parallel-plate PECVD of the thin-film silicon layers (Elettrorava S.p.A.). The (i)a-Si:H layers were deposited at 13.56 MHz (RF) via previously optimized bilayer recipe, combined with hydrogen plasma and 40.68 MHz (VHF) surface treatments.[2] Variations of the previously optimized 3-nm + 2-nm-thick (n)nc-Si:H + (n)a-Si:H stack were deposited to form the (n)-type CSPC as detailed in Section 2.2. All rear sides consisted of the previously optimized 5-nm + 30-nm-thick (p)nc-SiO$_x$:H + (p)nc-Si:H (p)-type CSPC.[8,21] Solar cell precursors were finalized by the front and rear deposition of 30- and 150-nm thick ITO via single-target RF magnetron sputtering (Polyteknic AS) at room temperature, respectively. After sputtering, the precursors were annealed at 180 °C for 5 min, and 3.92-cm^2 solar cells were formed via the Cu-electroplating metallization scheme previously developed.[19,20]

Front Contact Localization: The wet chemical patterning methods developed in Section 2.1 were conducted at room temperature using prepared baths of: analysis grade fuming HCl (37%) (Sigma Aldrich) (TCO etching), 14 mL HF (40%) (Merck) diluted in 1 L deionized (DI) water (interfacial oxide removal), and 12 g KOH (85%) pellets (Honeywell) diluted in 1 L DI water stirred at 300 RPM (thin-film silicon etching). Between baths, the samples were rinsed in a constant flow of DI water to prevent cross contamination between the solutions. A dedicated PECVD reactor (Elettrorava S.p.A.) was used for the full-area deposition of SiN$_x$:H at a temperature of 180 °C. A gas flow ratio of 5:45 SiH$_4$:NH$_4$ was used to ignite a plasma at 0.8 mbar with a power density of 42 mW cm^{-2}. Electron beam evaporation (Provac PRO500S) of MgF$_2$ in crystalline form was used to subsequently deposit the second ARC. Despite the full-area deposition of the ARC materials, the cells were contacted for characterization by physically removing these thin films from the busbar surrounding the cell.

Thin-Film and Solar Cell Characterization: The morphology of the localized front contacts was characterized using the SEM backscattered and secondary-electron detectors (Hitachi Regulus 8230). Effective minority carrier lifetime measurements on symmetric samples were measured using a photoconductance lifetime tester (Sinton WCT-120) in transient photoconductance decay mode. J–V characterization of solar cell samples was conducted with an AAA class solar simulator (WXS-90S-L2) using Kelvin probes to contact the samples to a source measure unit (Keithley 2601B). Additionally, pseudo-J–V measurements were made with an illumination-voltage tester (Sinton SunsV$_{oc}$-150) to extract R_S. The spectral response of the solar cell samples was evaluated using an in-house-built EQE, in conjunction with UV–vis–NIR spectrophotometry reflectance measurements (PerkinElmer Lambda 1050+) to evaluate the contributions lost to reflection. Spectroscopic ellipsometry (M-2000DI system, J.A. Woollam Co., Inc.) of the individual layers deposited on glass substrates was performed to obtain the n–k data used to perform optical simulations of the window opening regions of the solar cells with the GenPro4 simulation package.[40] The simulated absorptance, as well as the measured EQE and reflectance spectra, were integrated with the AM1.5G solar photon flux density distribution to obtain the reported contributions in terms of implied photocurrent density.[48]

Supporting Information

Supporting Information is available from the Wiley Online Library or from the author.

Acknowledgements

This research was performed at the Delft University of Technology, carried out by SolarLab part of SolarNL, a national research, innovation and industrial development program funded by the Netherlands National Growth Fund. Technical support was received from PVMD group technicians Martijn Tijssen, Engin Özkol, and Bernardus Zijlstra.

Conflict of Interest

The authors declare no conflict of interest.

Author Contributions

Sebastian Smits: data curation (lead); formal analysis (lead); investigation (equal); methodology (lead); writing—original draft (lead); writing—review & editing (lead). **Yifeng Zhao**: conceptualization (lead); investigation (equal); supervision (equal); writing—original draft (supporting); writing—review & editing (supporting). **Paul Procel Moya**: conceptualization (lead); investigation (equal); software (lead); writing—original draft (supporting); writing—review & editing (supporting). **Luana Mazzarella**: investigation (supporting); supervision (supporting); writing—original draft (supporting); writing—review & editing (supporting). **Olindo Isabella**: conceptualization (lead); funding acquisition (lead); investigation (equal); project administration (lead); supervision (equal); writing—original draft (supporting); writing—review & editing (supporting).

Data Availability Statement

The data that support the findings of this study are available from the corresponding author upon reasonable request.

Keywords

contact resistances, electron-selective contacts, localized contacts, silicon heterojunction solar cells, transparent conductive oxides

Received: December 20, 2024
Revised: January 15, 2025

[1] H. Lin, M. Yang, X. Ru, G. Wang, S. Yin, F. Peng, C. Hong, M. Qu, J. Lu, L. Fang, C. Han, P. Procel, O. Isabella, P. Gao, Z. Li, X. Xu, *Nat. Energy* **2023**, *8*, 789.

[2] Y. Zhao, P. Procel, A. Smets, L. Mazzarella, C. Han, G. Yang, L. Cao, Z. Yao, A. Weeber, M. Zeman, O. Isabella, *Prog. Photovoltaics* **2023**, *31*, 1170.

[3] Y. Zhao, P. Procel, C. Han, L. Cao, G. Yang, E. Özkol, A. Alcañiz, K. Kovačević, G. Limodio, R. Santbergen, A. Smets, A. Weeber, M. Zeman, L. Mazzarella, O. Isabella, *Sol. Energy Mater. Sol. Cells* **2023**, *258*, 112413.

[4] Z. C. Holman, A. Descoeudres, L. Barraud, F. Z. Fernandez, J. P. Seif, S. De Wolf, C. Ballif, *IEEE J. Photovoltaics* **2012**, *2*, 7.

[5] Z. C. Holman, M. Filipič, A. Descoeudres, S. De Wolf, F. Smole, M. Topič, C. Ballif, *J. Appl. Phys.* **2013**, *113*, 013107.

[6] R. V. K. Chavali, S. De Wolf, M. A. Alam, *Prog. Photovoltaics* **2018**, *26*, 241.

[7] Y. Liu, Y. Li, Y. Wu, G. Yang, L. Mazzarella, P. Procel-Moya, A. C. Tamboli, K. Weber, M. Boccard, O. Isabella, X. Yang, B. Sun, *Mater. Sci. Eng.: R: Rep.* **2020**, *142*, 100579.

[8] Y. Zhao, L. Mazzarella, P. Procel, C. Han, F. D. Tichelaar, G. Yang, A. Weeber, M. Zeman, O. Isabella, *Prog. Photovoltaics* **2022**, *30*, 809.

[9] Y. Zhao, L. Mazzarella, P. Procel, C. Han, G. Yang, A. Weeber, M. Zeman, O. Isabella, *Prog. Photovoltaics* **2020**, *28*, 425.

[10] P. Procel, G. Yang, O. Isabella, M. Zeman, *Sol. Energy Mater. Sol. Cells* **2018**, *186*, 66.

[11] R. Kopecek, F. Buchholz, V. D. Mihailetchi, J. Libal, J. Lossen, N. Chen, H. Chu, C. Peter, T. Timofte, A. Halm, Y. Guo, X. Qu, X. Wu, J. Gao, P. Dong, *Solar* **2023**, *3*, 1.

[12] H. Tang, H. Lin, G. Wang, Q. Su, T. Wang, C. Xue, L. Fang, X. Xu, C. Han, P. Gao, *Prog. Photovoltaics* **2024**.

[13] M. Bivour, S. Schröer, M. Hermle, S. W. Glunz, *Sol. Energy Mater. Sol. Cells* **2014**, *122*, 120.

[14] J. Haschke, O. Dupré, M. Boccard, C. Ballif, *Sol. Energy Mater. Sol. Cells* **2018**, *187*, 140.

[15] J. Haschke, G. Christmann, C. Messmer, M. Bivour, M. Boccard, C. Ballif, *J. Appl. Phys.* **2020**, *127*, 114501.

[16] S. Li, M. Pomaska, A. Lambertz, W. Duan, K. Bittkau, D. Qiu, Z. Yao, M. Luysberg, P. Steuter, M. Köhler, K. Qiu, R. Hong, H. Shen, F. Finger, T. Kirchartz, U. Rau, K. Ding, *Joule* **2021**, *5*, 1535.

[17] H. Sai, T. Matsui, *Sol. RRL* **2023**, *7*, 2300290.

[18] M. Boccard, L. Antognini, J. Cattin, J. Dréon, W. Lin, V. Paratte, D. Turkay, C. Ballif, *IEEE J. Photovoltaics* **2023**, *13*, 663.

[19] G. Limodio, Y. De Groot, G. Van Kuler, L. Mazzarella, Y. Zhao, P. Procel, G. Yang, O. Isabella, M. Zeman, *IEEE J. Photovoltaics* **2020**, *10*, 372.

[20] C. Han, G. Yang, P. Procel, D. O'Connor, Y. Zhao, A. Gopalakrishnan, X. Zhang, M. Zeman, L. Mazzarella, O. Isabella, *Sol. RRL* **2022**, *6*, 2100810.

[21] Y. Zhao, P. Procel, C. Han, L. Mazzarella, G. Yang, A. Weeber, M. Zeman, O. Isabella, *Sol. Energy Mater. Sol. Cells* **2021**, *219*, 110779.

[22] M. Scholten, J. E. A. M. van den Meerakker, *J. Electrochem. Soc.* **1993**, *140*, 471.

[23] ASTM D3359-23, *Standard Test Methods for Rating Adhesion by Tape Test*, ASTM International, West Conshohocken, PA, USA **2023**.

[24] J. E. A. M. van den Meerakker, P. C. Baarslag, M. Scholten, *J. Electrochem. Soc.* **1995**, *142*, 2321.

[25] T.H. Tsai, Y.F. Wu, *Microelectron. Eng.* **2006**, *83*, 536.

[26] T. M. Pan, T. F. Lei, F. H. Ko, T. S. Chao, T. H. Chiu, Y. H. Lee, C. P. Lu, *IEEE Trans. Semicond. Manuf.* **2001**, *14*, 365.

[27] S. S. Mammana, A. Greatti, F. H. Luiz, F. I. da Costa, A. P. Mammana, G. A. Calligaris, L. P. Cardoso, C. I. Z. Mammana, D. den Engelsen, *Thin Solid Films* **2014**, *567*, 20.

[28] S. M. Greil, N. Mingirulli, L. Korte, K. Hartmann, A. Schöpke, J. Rappich, B. Rech, *Energy Procedia* **2011**, *8*, 269.

[29] C. Zhou, J. Li, L. Wu, G. Guo, H. Wang, P. Chen, B. Yu, L. Qian, *RSC Adv.* **2018**, *8*, 36043.

[30] W. Luo, Y. Sheng Khoo, P. Hacke, V. Naumann, D. Lausch, S. P. Harvey, J. Prakash Singh, J. Chai, Y. Wang, A. G. Aberle, S. Ramakrishna, *Energy Environ. Sci.* **2017**, *10*, 43.

[31] C. Leendertz, N. Mingirulli, T. F. Schulze, J. P. Kleider, B. Rech, L. Korte, *Appl. Phys. Lett.* **2011**, *98*, 202108.

[32] J. Bao, A. Liu, Y. Lin, Y. Zhou, *Mater. Chem. Phys.* **2020**, *255*, 123625.

[33] D. Zhang, I. A. Digdaya, R. Santbergen, R. A. C. M. M. van Swaaij, P. Bronsveld, M. Zeman, J. A. M. van Roosmalen, A. W. Weeber, *Sol. Energy Mater. Sol. Cells* **2013**, *117*, 132.

[34] Z. Yang, H. Lin, K. W. A. Chee, P. Gao, J. Ye, *Nano Energy* **2019**, *61*, 221.

[35] C. Han, Y. Zhao, L. Mazzarella, R. Santbergen, A. Montes, P. Procel, G. Yang, X. Zhang, M. Zeman, O. Isabella, *Sol. Energy Mater. Sol. Cells* **2021**, *227*, 111082.

[36] D. Pysch, A. Mette, S. W. Glunz, *Sol. Energy Mater. Sol. Cells* **2007**, *91*, 1698.

[37] A. Richter, V. Smirnov, A. Lambertz, K. Nomoto, K. Welter, K. Ding, *Sol. Energy Mater. Sol. Cells* **2018**, *174*, 196.

[38] L. Mazzarella, S. Kirner, O. Gabriel, S. S. Schmidt, L. Korte, B. Stannowski, B. Rech, R. Schlatmann, *Phys. Status Solidi A* **2017**, *214*, 1532958.

[39] M. Boccard, R. Monnard, L. Antognini, C. Ballif, *AIP Conf. Proc.* **2018**, *1999*, 040003.

[40] R. Santbergen, T. Meguro, T. Suezaki, G. Koizumi, K. Yamamoto, M. Zeman, *IEEE J. Photovoltaics* **2017**, *7*, 919.

[41] C. Xu, O. Isabella, M. R. Vogt, *Resour. Conserv. Recycl.* **2024**, *210*, 107824.

[42] P. Procel-Moya, Y. Zhao, O. Isabella, *Sol. Energy Mater. Sol. Cells* unpublished.

[43] F. T. Thome, P. Meßmer, S. Mack, E. Schnabel, F. Schindler, W. Kwapil, M. C. Schubert, *Sol. RRL* **2024**, *8*, 2400628.

[44] B. Xu, K. Bittkau, A. Eberst, K. Zhang, Y. Liu, J. Yang, W. Duan, M. A. Yaqin, V. Smirnov, C. Zhou, W. Wang, X. Xu, A. Lambertz, U. Rau, K. Ding, *Adv. Energy Sustainability Res.* **2024**, 2400227.

[45] A. Sinha, J. Qian, S. L. Moffitt, K. Hurst, K. Terwilliger, D. C. Miller, L. T. Schelhas, P. Hacke, *Prog. Photovoltaics* **2023**, *31*, 36.

[46] G. Yang, P. Guo, P. Procel, G. Limodio, A. Weeber, O. Isabella, M. Zeman, *Solar Energy Mater. Sol. Cells* **2018**, *186*, 9.

[47] D. Deligiannis, S. Alivizatos, A. Ingenito, D. Zhang, M. van Sebille, R. A. C. M. M. van Swaaij, M. Zeman, *Energy Procedia* **2014**, *55*, 197.

[48] ASTM G173-23, Tables for Reference Solar Spectral Irradiances: Direct Normal and Hemispherical on 37 Tilted Surface, ASTM International, West Conshohocken, PA, USA 2023.